

# Ion-mediated RNA structural collapse: effect of spatial confinement

Zhi-Jie TAN<sup>1\*</sup> and Shi-Jie CHEN<sup>2\*</sup>

<sup>1</sup>Department of Physics and Key Laboratory of Artificial Micro & Nano-structures of Ministry of Education, School of Physics and Technology, Wuhan University, Wuhan, P.R. China 430072

<sup>2</sup>Department of Physics and Astronomy and Department of Biochemistry, University of Missouri, Columbia, MO 65211

## Abstract

RNAs are negatively charged molecules residing in macromolecular crowding cellular environments. Macromolecular confinement can influence the ion effects in RNA folding. In this work, using the recently developed tightly bound ion model for ion fluctuation and correlation, we investigate the confinement effect on the ion-mediated RNA structural collapse for a simple model system. We found that, for both  $\text{Na}^+$  and  $\text{Mg}^{2+}$ , ion efficiencies in mediating structural collapse/folding are significantly enhanced by the structural confinement. Such an enhancement in the ion efficiency is attributed to the decreased electrostatic free energy difference between the compact conformation ensemble and the (restricted) extended conformation ensemble due to the spatial restriction.

---

Running title: Ion-mediated RNA collapse and crowding effect

\*Emails: chenshi@missouri.edu (to S.J.C.); zjtan@whu.edu.cn (to Z.J.T.).

Keywords: RNA folding, ion electrostatics, macromolecular crowding, tightly bound ion model

## Introduction

Cellular functions of nucleic acids are intrinsically related to their folding in cellular environments (1–3). Since DNAs/RNAs are highly negatively charged molecules, folding into compact native structures requires metal ions to overcome the strong Coulombic repulsions (1)–(13). Furthermore, RNAs *in vivo* are surrounded by many other molecules (14–16), and the volume percentage of macromolecules in cells can reach 40% (14–16). The presence of other macromolecules around an RNA can cause spatial confinement for DNA/RNAs folding. The macromolecular crowding may greatly influence the RNA folding (17–21). However, the problem of how the spatial constraint affects the ion-induced RNA folding is not fully solved. In this work, we will construct a simplified structural model to investigate the macromolecular crowding effect on ion-mediated RNA collapse/folding.

For RNA secondary structure folding (1–3), the thermodynamic parameters at standard salt condition (namely, 1M Na<sup>+</sup>), have been experimentally determined. Parameters for other ionic conditions have also been fitted from experimental data and theoretical calculations (22)–(33). These parameters have led to many accurate predictions for RNA/DNA secondary structures and folding kinetics (22)–(33). For tertiary structure folding, however, our understanding of the role of ions, especially the effects of multivalent ions such as Mg<sup>2+</sup>, remains incomplete (1)–(13). Experimental and computational studies showed that metal ions with higher charge density are more efficient in promoting RNA collapse and stronger ion-correlations could potentially contribute to the efficient role of Mg<sup>2+</sup> ions (34)–(40). Another series of experiments for short DNA helices suggested the existence of helix-helix attractive force at high multivalent ion concentration and repulsive force at low ion concentration (41, 42). Furthermore, experiments on a paradigm system consisting of two helices tethered by a loop suggested that Mg<sup>2+</sup> is >10-fold more efficient than the predictions from the Poisson-Boltzmann (PB) theory in promoting structural collapse (43–45).

In the cells, the presence of other molecules can cause a crowded environment that can cause spatial confinement for the conformations of RNAs and consequently influence the free energy landscape of RNAs. For proteins, macromolecular crowding has been shown to play an important role in folding stability, structure, and kinetics (14, 15, 46–51). For RNAs, however, the study of macromolecular crowding effect on folding is relatively new (52), especially on its impact on the role of ions in folding (19).

RNA tertiary structure collapse involves high charge density, quantitative description for the role of metal ions is challenging, especially for multivalent ions. Molecular dynamics studies for ion-RNA interactions have provided novel insights into ion and structure/sequence-specific forces in RNA folding, especially the force arising from site-specific binding of ions (53)–(58). The two classic polyelectrolyte theories: the counterion condensation (CC) theory (59) and the PB theory (60)–(65) have been successful in predicting electrostatic properties of biomolecules (59)–(65). However, for the complex RNA tertiary structures, the line-charge structural model used in the CC theory could be oversimplified (59). Furthermore, RNAs with high charge density generally induce high ion concentration and consequently could possibly cause ion-ion correlations for multivalent ions in the vicinity of RNA surface. The PB theory ignores such potentially important effects for multivalent ion solutions (66–68). In order to take into account the effects of ion correlations and ion-binding ensemble, the tightly bound ion (TBI) model was developed (66, 67); see the Supplementary Material for an introduction of the TBI model. Experimental comparisons sug-

gest that the TBI model may offer improved predictions on the ion effect of thermodynamic stability of DNA/RNA helices/hairpins (31–33), DNA helix assembly (69–71), and ion-binding properties and tertiary folding stability of RNAs in the presence of  $Mg^{2+}$  (72–74).

In this work, we will employ the newly refined TBI model (72, 73) to investigate a paradigm system with two nucleic acid helices tethered by a loop. We will focus on the effect of conformational constraint on the role of ions in RNA folding. The conformational constraint can arise from the macromolecular crowding effect. Moreover, the study goes far beyond the previous studies which only involves planar configurations (70). Specifically, we will consider the conformational fluctuation of helices at the all-atom level with 3-dimensional rotations and compare our predictions with the recent experimental data as well as the predictions from the PB theory (44),

## Methods

### Structural model

The model system consists of two helices tethered by a flexible loop; see Fig. 1. In the model, we allow for three-dimensional rotation of the helix axes. We note that in a previous study, only symmetric co-planar model rotations were allowed (70). As shown in Fig. 1, a configuration of the system can be constructed through the following operations. First, the two parallel helices are separated by a axis-axis distance  $x$ ; Second, the two helices are symmetrically rotated around the respective ends (O and O') of the helix axis in the axis-axis plane with an angle  $\theta$ ; Third, the two helices are rotated so that the projections of two helix axes in the plane perpendicular to line of O-O' are separated by an angle  $\gamma$ . The configuration of the system can be described by three parameters: the distance  $x$ , the angles  $\theta$  and  $\gamma$ . Here, the parameter  $\gamma$  is used to produce non-planar configurations. The (DNA) helices here are assumed to adopt the B-form structure (75). We use the intervals of ( $3\text{\AA}$ ,  $20^\circ$ ,  $20^\circ$ ) to sample the conformational space of ( $x \in [5\text{\AA}, 56\text{\AA}]$ ,  $\theta \in [0, 180^\circ]$ ,  $\gamma \in [0, 180^\circ]$ ). To reduce the computational time, we randomly select  $\sim 600$  configurations from the full 3D conformation ensemble for calculations. Tests with the different sampling show that our results are quite robust. In the structural model, the three parameters ( $x$ ,  $\theta$ ,  $\gamma$ ) are used to produce the major portion of the full conformational ensemble, including the non-planar/planar and compact/extended conformational ensembles. Although this approximation may be valid as we focus on the low-resolution energy landscape of the system, it would be useful in further studies to examine the effects of other degrees of freedoms such as the spin of helices and asymmetrical rotations of helix axes.

### Free energy

For a given configuration of the system described by  $(x, \theta, \gamma)$ , the total free energy  $G(x, \theta, \gamma)$  can be calculated as

$$G(x, \theta, \gamma) = G_E(x, \theta, \gamma) + G_{\text{loop}}(x, L) + G_{\text{cs}} + G_{3^\circ}, \quad (1)$$

where  $G_E(x, \theta, \gamma)$  is the electrostatic free energy for the two helices in an ionic solution.  $G_{\text{loop}}(x, L)$  is the free energy of the loop.  $G_{\text{cs}}$  is the coaxial stacking free energy between the two helices, and  $G_{3^\circ}$  is the

tertiary contact energy as the two helices are in close contact.

In the study, we calculate  $G_E(x, \theta, \gamma)$  using the all-atom TBI model (72, 73); see the Supplemental Information for a detailed description of the model. We calculate  $G_{\text{loop}}(x, L)$  from

$$G_{\text{loop}} = -k_B T \ln P_{\text{loop}}(x, L), \quad (2)$$

where  $P_{\text{loop}}(x, L)$  is the probability of a loop of length  $L$  with end-to-end distance  $x$ .  $P_{\text{loop}}(x, L)$  can be estimated from an approximate analytical expression (76):  $P_{\text{loop}}(x, L) = \frac{4\pi A(x/L)^2}{(1-(x/L)^2)^{9/2}} \exp\left(\frac{-3L/l_p}{4(1-(x/L)^2)}\right)$ , where  $A$  is the normalization constant (76–78) and  $l_p$  is the persistence length of the loop. In our calculations, in order to make direct comparison with the experiment, we assume that the loop is a PEG chain (44) and the persistence length is  $3.8\text{\AA}$  (44, 70).

The coaxial stacking free energy term  $G_{\text{cs}}$  is an important energetic factor for nucleic acid helix alignment (28, 79). We model this term based on the thermodynamic parameters (23, 79) and the RNA structure analysis (28)

$$G_{\text{cs}} = G_0 \text{ for } x < 10\text{\AA} \text{ and } \theta > 150^\circ; \quad (3)$$

$$= 0 \text{ else,} \quad (4)$$

where  $G_0 = G_{\frac{\text{XX}}{\text{XX}}} - \delta g$ . Here,  $\frac{\text{XX}}{\text{XX}}$  is the coaxial stacked base pairs, and  $G_{\frac{\text{XX}}{\text{XX}}} = -1.5 \text{ kcal/mol}$  for  $\frac{\text{CT}}{\text{GA}}$  (at  $25^\circ\text{C}$ ) in the experimental system (44).  $\delta g (\approx -1 \text{ kcal/mol})$  is an offset between the coaxial stacking energy and the corresponding canonical base pairs (79).

$G_{3^\circ}$  is added to account for the possible tertiary contacts (45)

$$G_{3^\circ} = g_{3^\circ} \text{ for } R_{\text{cc}} \leq 28\text{\AA}; \quad (5)$$

$$= 0 \text{ else,} \quad (6)$$

where  $g_{3^\circ}$  is a constant negative energy. In the calculation, we use  $-10k_B T$ ,  $-12k_B T$ , and  $-14k_B T$  to investigate the effect of the tertiary contact, respectively. We use the condition  $R_{\text{cc}} \leq 28\text{\AA}$ , a typical inter-axial distance for ion-induced DNA aggregates (80–83), to simulate a close contact where tertiary contact can occur. Our control tests show that the small changes in the criteria around  $28\text{\AA}$  would not cause significant changes in our quantitative predictions or qualitative conclusions.

For the purpose of visualizing the free energy landscape, we will also use the inter-axis angle  $\Theta$  to represent the two angles  $\theta$  and  $\gamma$  (shown in Fig. 1)

$$\Theta = \arccos\left(\cos^2\left(\frac{\theta}{2}\right)\cos^2\left(\frac{\gamma}{2}\right)\right), \quad (7)$$

to show the electrostatic free energy landscape in 2D  $(x, \Theta)$  plane instead of in 3D  $(x, \theta, \gamma)$  space.

## Spatial confinement

As shown in Fig. 1, we use  $R_{\text{cc}}$ , the distance between the centers of the two axes of the helices, to describe the compactness of the system. Furthermore, we use the distance between the outer axial ends

$R_{PP'} \leq R_{\max}$ , to quantify the spatial constraint of the system. A smaller  $R_{\max}$  corresponds to a stronger spatial confinement due to, for example, macromolecular crowders.

To quantify the compactness of the system for an ensemble of conformations, we use a Boltzmann-weighted averaged value  $\bar{R}_{cc}$  for the distance  $R_{cc}$  between the centers of the helix pair (70)

$$\bar{R}_{cc} = \frac{\sum_{(x,\theta,\gamma)} R_{cc} e^{-G(x,\theta,\gamma)/k_B T}}{\sum_{(x,\theta,\gamma)} e^{-G(x,\theta,\gamma)/k_B T}}. \quad (8)$$

## Results and Discussions

To investigate how the different ionic conditions affect the folding properties of the model system, we apply the TBI model to calculate the electrostatic free energy landscape for a wide range of  $\text{Na}^+$  and  $\text{Mg}^{2+}$  conditions:  $[\text{Mg}^{2+}] \in [0.01\text{mM}, 0.1\text{M}]$  and  $[\text{Na}^+] \in [0\text{M}, 2\text{M}]$ . To directly simulate the experiments (44), we assume that the system is always immersed in a 16mM  $\text{Na}^+$  background (from the Na-MOPS buffer). For convenience, we define the following two specific states for the model system: (i) the random relaxation state where the two helices can fluctuate randomly, corresponding to the state with fully neutralized helices (43, 44); (ii) the (electrostatically) folded (collapsed) state with  $\bar{R}_{cc} \leq 30\text{\AA}$  (3, 69, 80–83).

In the following, we will first present the results on the electrostatic free energy landscape. We will then discuss the role of ions in the structural collapse (without the possible tertiary contact). Finally, we will discuss the effects of spatial confinement and tertiary contacts on the ion role in structural folding.

### Electrostatic free energy landscape

#### *In $\text{Na}^+$ solutions.*

Figs. 2A-D show the electrostatic free energy landscape  $G_E$  for the different added  $[\text{Na}^+]$ . At low added  $[\text{Na}^+]$ , the helices tend to avoid each other with the largest  $x$  and  $\Theta$  (see Fig. 2A) due to the weak charge neutralization. An increased  $[\text{Na}^+]$  would enhance the ion binding and charge neutralization due to a lower entropic penalty for ion-binding, thus causing a weakened inter-helix repulsion. As shown in Fig. 2B, the helices fluctuate around less extended conformations with smaller  $x$  and  $\Theta$  values. When  $[\text{Na}^+]$  becomes very high ( $> 0.3\text{M}$ ), the helices become nearly fully neutralized, thus the helices can fluctuate randomly in the full conformational space (see Figs. 2CD), except for very compact configurations (very small  $x$  and  $\Theta$ ) where helix-helix and ion-helix exclusions play a dominate role.

#### *In $\text{Mg}^{2+}$ solutions.*

Figs. 2E-H show the electrostatic free energy landscapes  $G_E$  for the helices with the different added  $[\text{Mg}^{2+}]$ . At low  $[\text{Mg}^{2+}]$ , the helices form extended conformations with large  $x$  and  $\Theta$ . With the increase of  $[\text{Mg}^{2+}]$ , the two helices switch to the conformations with smaller  $\Theta$  and  $x$  (Figs. 2FG). For high  $[\text{Mg}^{2+}]$  ( $> 3\text{mM}$ ), the helices tend to adopt the conformations with very small  $\Theta$  ( $\Theta \lesssim 40^\circ$ ) and intermediate  $x$  ( $32\text{\AA} \lesssim x \lesssim 47\text{\AA}$ ); see Fig. 2H. The above transition with increasing  $[\text{Mg}^{2+}]$  can be attributed to the divalent ion-mediated helix-helix interactions (43, 69, 70). When  $[\text{Mg}^{2+}]$  is very low, background  $\text{Na}^+$  of low concentration in buffer only gives weak neutralization to helices, thus the helices repel each other and

the conformations with largest  $x$  and  $\Theta$  would be favorable. With the increase of  $[\text{Mg}^{2+}]$ ,  $\text{Mg}^{2+}$  will compete with background  $\text{Na}^+$ , and the self-organization of  $\text{Mg}^{2+}$  could induce (slight) attractive force between helices (69, 70). Such attraction would become stronger for the helix-helix near-parallel configurations at intermediate separation and at higher  $[\text{Mg}^{2+}]$  (70). As a result, the helices would transform to the conformations with small  $\Theta$  and intermediate  $x$  (69).

Compared with the results for 2D (co-planar) configurations (Fig. 2 in Ref (70)), more extended conformations (large  $\Theta$ ) are shown in the current 3D free energy landscapes, causing an increase in the conformational entropy of the two helices and weakening the effect of the possible  $\text{Mg}^{2+}$ -mediated helix-helix attractive force in the structural collapse.

### **Ion-mediated structural collapse: without spatial confinement**

First, we discuss the role of ions in the structural collapse without spatial confinement and tertiary contact by setting  $G_{3^0} = 0$  in Eq. 1. In the following, we present general features for the system and the comparisons with the experimental data (44).

#### *General features*

As shown in Fig. 3A, with the increase of  $[\text{Na}^+]$  to  $2M$ ,  $\bar{R}_{\text{cc}}$  decreases from a large value to that of the random relaxation (fully neutralized) state. Such a trend of  $\bar{R}_{\text{cc}}$  is a results of the electrostatic free energy landscapes shown in Fig. 2A-D and can be attributed to the aforementioned enhanced  $\text{Na}^+$ -binding at higher  $[\text{Na}^+]$ . Also shown in Fig. 3A is the loop length dependence of the structural compaction at low and high  $[\text{Na}^+]$ . A PEG chain is quite flexible ( $l_p \simeq 3.8\text{\AA}$ ). The loop (length  $L \gg l_p$ ) tends to minimize the loop entropic loss upon structure formation. Therefore, the loop drives the system to fluctuate around a relatively smaller end-to-end distance  $x$  since a larger  $x$  corresponds to a smaller loop entropy. For example, for PEG loops with  $L = 56\text{\AA}$  and  $32\text{\AA}$ ,  $x \simeq 20\text{\AA}$  and  $15\text{\AA}$ , are the most favorable according to Eq. 2, respectively. The loop effect is slightly stronger for low  $[\text{Na}^+]$  where the favorable configurations are extended and the effect of the (short) tether can become more important.

In a solution with added  $[\text{Mg}^{2+}]$ , at low  $[\text{Mg}^{2+}]$ , the favorable conformations are those with large  $x$  and  $\Theta$ , thus a loop length can contribute to the compaction of the system. In contrast, at a high  $[\text{Mg}^{2+}]$ ,  $\text{Mg}^{2+}$  induces (slightly) attractive force between helices at small inter-axis angles  $\Theta$  (see Fig. 2H). When the helices are driven by the loop to a smaller  $x$  (to gain loop conformation entropy), the low free energy conformations (in the small  $x$  regime in Figs. 2GH) correspond to a range of  $\Theta$ . As a result, a small  $x$  does not necessarily lead to compaction of the system (characterized by a small  $\bar{R}_{\text{cc}}$ ). We note that a high  $[\text{Mg}^{2+}]$  can induce a state that is slightly more compact than the random relaxation (fully neutralized) state yet much looser than the upper limit of the electrostatically folded state (3, 80–83), as shown in Fig. 3B.

#### *Comparisons with experiments*

To make direct comparison with the experimental system (44), we assume the loop length to be  $L = 32\text{\AA}$ . We calculated the Boltzmann-weighted averaged SAXS profiles  $I(Q)$  over conformation ensemble for each ionic condition. Here  $Q$  is the scattering vector which is equal to  $4\pi \sin(\vartheta)/\lambda$ , where  $\vartheta$  is the Bragg angle



and  $\lambda$  is the wave length of the radiation.

Figs. 3C&D show the SAXS profiles for the different added  $[\text{Na}^+]$  and  $[\text{Mg}^{2+}]$ , respectively. As the added  $[\text{Na}^+]$  is increased from 0 to 2M or  $\text{Mg}^{2+}$  is added from 0 to 0.1M, the SAXS profile changes from that of the extended state to that of the nearly fully neutralized state. In addition, the profiles indicate that the system at high  $[\text{Mg}^{2+}]$  ( $\sim 0.1\text{M}$ ) is slightly more compact than that at high  $[\text{Na}^+]$  ( $\sim 2\text{M}$ ). Since the experimental SAXS profiles are in arbitrary unit and with vertical shifts (44), we cannot make direct comparisons for the SAXS profiles between the experiments and our predictions.

Based on the calculated SAXS profiles and compactness  $\bar{R}_{\text{cc}}$ , we can estimate the fraction “relaxed”  $\chi$  for the system by (44)

$$\Omega(\text{Na}^+ \text{ or } \text{Mg}^{2+}) = (1 - \chi) \Omega(\text{no added salt}) + \chi \Omega(\text{high salt}), \quad (9)$$

where  $\Omega$  stands for a structural parameter, such as  $I(Q)$  or  $\bar{R}_{\text{cc}}$ .  $\Omega(\text{no added salt})$  is that in 16mM  $\text{Na}^+$  background from the Na-MOPS buffer without added salt, and  $\Omega(\text{high salt})$  is taken as that of the fully-neutralized state in our estimation. Based on the equation, we estimate  $\chi$  from the calculated  $I(Q)$  and  $\bar{R}_{\text{cc}}$  respectively, and compare our predictions with experiments for the cases with added  $\text{Na}^+$  and  $\text{Mg}^{2+}$ .

Figs. 3E&F show the fraction “relaxed”  $\chi$  as a function of added  $[\text{Na}^+]$  and  $[\text{Mg}^{2+}]$ , respectively. When  $[\text{Na}^+]$  is added,  $\chi$  increases from zero to  $\sim 0.9$  at 2M  $[\text{Na}^+]$ , suggesting that the system is close to the random relaxation (fully neutralized) state. The lines estimated from  $I(Q)$  and  $\bar{R}_{\text{cc}}$  are almost identical, and the predictions agree well with the experimental data, as shown in Fig. 3E.

As shown in Fig. 3F, when  $\text{Mg}^{2+}$  is added,  $\chi$  increases from zero to  $\sim 0.9$  at  $\sim 8\text{mM}$   $[\text{Mg}^{2+}]$ , and may slightly exceeds 1 when  $[\text{Mg}^{2+}] \gtrsim 10\text{mM}$ , suggesting slightly more compact state induced by high  $[\text{Mg}^{2+}]$ . In addition, the predicted  $\chi$  from  $\bar{R}_{\text{cc}}$  is slightly larger than that from  $I(Q)$  at high  $[\text{Mg}^{2+}]$  (shown in Fig. 3F), which is in accordance with the above described relations of  $\bar{R}_{\text{cc}}$  and  $I(Q)$  with  $[\text{Na}^+]$  and  $[\text{Mg}^{2+}]$ . Fig. 3F also shows that the predicted  $\chi$ 's from the TBI model are in good accordance with the experimental data, while PB theory predicts  $>10$ -fold higher midpoint of  $[\text{Mg}^{2+}]$  for the  $\text{Mg}^{2+}$ -mediated collapse. This result may be attributed to the ignored ion-ion correlations in the PB. The inclusion of ion correlations would allow ions to self-organize to form low-energy state, and thus the TBI model predicts a more efficient role of  $\text{Mg}^{2+}$  than the PB (67, 72, 73).

It is important to note that although the system has the similar global compactness at high  $[\text{Na}^+]$  and  $[\text{Mg}^{2+}]$ , the free energy landscapes are very different as shown in Fig. 2.

The PEG loop used in the above calculation is electrically neutral, while a realistic RNA loop is a polyanionic chain. Recent experiments suggest that the hinge stiffness can become an energetic barrier for RNA folding (39). As shown previously (70), a nucleotide loop may enhance the sharpness of ion-mediated structural collapse due to the ion-dependence of the persistence length of the loop (e.g., (70)).

### **Ion-mediated folding: with spatial confinement**

In this section, we investigate the influence of spatial restriction as well as a tertiary contact on the ion-mediated collapse of the above two-helix system.

*Electrostatic free energy landscape with spatial confinement.*

With the conformational confinement defined by the limit  $R_{\max}$  for the distance  $R_{PP'}$  between the outer ends of the two helices (see Fig. 1), the conformational space of the system is confined. The electrostatic free energy landscape of the confined system  $G_E(R_{cc}, R_{\max})$  is given by

$$G_E(R_{cc}, R_{\max}) = -k_B T \ln \sum_{R_{cc}}^{R_{PP'} \leq R_{\max}} e^{-G_E(x, \theta, \gamma)/k_B T}, \quad (10)$$

where  $R_{cc}$  is the distance between the two centers of the two helices (see Fig. 1).

As shown in Fig. 4, the spatial restriction influences the free energy landscape significantly for both  $\text{Na}^+$  and  $\text{Mg}^{2+}$  solutions. For large  $R_{\max}$ , the free energy landscape is close to that without spatial restriction. At low  $[\text{Na}^+]$ , the favorable conformations are clustered in the region of large  $R_{cc}$ . At high  $[\text{Na}^+]$  (e.g., 2M), the helices can fluctuate nearly in the whole region with all the different  $R_{cc}$  values. With the decrease of  $R_{\max}$ , the conformations of the two helices are confined by the restriction and the extended conformations are severely limited. This causes the free energy  $G_E(R_{cc}, R_{\max})$  at high  $[\text{Na}^+]$  to become close to that at low  $[\text{Na}^+]$ . In the limit of strong spatial confinement such as  $R_{\max} \leq 40\text{\AA}$ , the free energy  $G_E(R_{cc}, R_{\max})$  at the different  $\text{Na}^+$  concentrations can become nearly identical; see Figs. 4A-D in the small  $R_{\max}$  regime.

For  $\text{Mg}^{2+}$  solutions, the spatial confinement effect on  $G_E(R_{cc}, R_{\max})$  is similar to that for  $\text{Na}^+$  solutions, except for the much more efficient role of the  $\text{Mg}^{2+}$  ions in promoting the collapse of the system. The electrostatic free energy landscapes show that with the spatial confinement, the extended conformations are much more significantly restricted than the compact conformations, causing the destabilization of the extended state. In the ion-promoted collapse, the spatial confinement would effectively enhance the ion effect in folding.

*Ion-mediated folding: effects of spatial confinement and tertiary contacts*

To investigate the role of tertiary contacts in ion-induced structural collapse, we add a negative constant energy to model the effect of the tertiary contacts. Specifically, we choose three values  $-10k_B T$ ,  $-12k_B T$ , and  $-14k_B T$  for  $g_{3^\circ}$  (see Eq. 6).

Helix-helix attraction arising from the tertiary contacts would cause a shift in the conformational distribution toward the compact state and lower the ion concentration required to induce the collapse of the structure. Furthermore, the tertiary contact results in a much sharper ion-induced structural collapse (than the tertiary contact-free case). The effect is more pronounced for stronger tertiary contacts. As shown in Figs. 5ACE for  $\text{Na}^+$ , the midpoint for the folding transition occurs at  $[\text{Na}^+] \sim 0.5\text{M}$  for  $g_{3^\circ} = -10k_B T$  and  $[\text{Na}^+] \sim 0.08\text{M}$  for  $g_{3^\circ} = -14k_B T$ , respectively, and the stronger tertiary contacts cause a slightly more compact state. As shown in Figs. 5BDF, the midpoints of of  $\text{Mg}^{2+}$ -dependent folding are  $\sim 0.8\text{mM}$  and  $\sim 0.2\text{mM}$  for  $g_{3^\circ} = -10k_B T$  and  $g_{3^\circ} = -14k_B T$ , respectively. Again, we note that much lower  $[\text{Mg}^{2+}]$  ( $\sim \text{mM}$ ) is required to cause folding than  $[\text{Na}^+]$  ( $\sim \text{M}$ ), which is in accordance with the experimental data (13, 34, 72, 73).

To further examine the effect of the spatial confinement in the presence of tertiary contacts, we calculated  $\bar{R}_{cc}$  with a given  $R_{\max}$  constraint (the maximum distance of P-P' shown in Fig. 1). As shown in Figs. 5A-F, the spatial confinement significantly enhances the ion efficiency in mediating the structural collapse/folding



in both  $\text{Na}^+$  and  $\text{Mg}^{2+}$  solutions. For example, for  $g_{3^\circ} = -10k_B T$ , with the decrease of  $R_{\max}$  from  $120\text{\AA}$  to  $70\text{\AA}$ , the  $[\text{Na}^+]$  and  $[\text{Mg}^{2+}]$  at the midpoint of the folding transition decreases from  $\sim 0.5\text{M}$  to  $\sim 0.1\text{M}$  and from  $\sim 1\text{mM}$  to  $\sim 0.3\text{mM}$ , respectively. For a stronger tertiary contact, e.g.,  $g_{3^\circ} = -14k_B T$ , the spatial confinement would further enhance the ion efficiency for both of  $\text{Na}^+$  and  $\text{Mg}^{2+}$ , as shown in Figs. 5A-F. Such higher efficiency of  $\text{Mg}^{2+}$  than  $\text{Na}^+$  is attributed to the higher valence of  $\text{Mg}^{2+}$  which corresponds to the less entropy for ion binding and stronger ion-ion correlation, causing higher  $\text{Mg}^{2+}$  binding affinity (72) and consequently higher efficiency in stabilizing RNA (73).

The above spatial confinement-promoted ion ( $\text{Na}^+$  and  $\text{Mg}^{2+}$ ) efficiency in mediating structural folding is in accordance with the recent experiment which showed that a lower  $\text{Mg}^{2+}$  is required to fold *Azoarcus* ribozyme in PEG environments (19). The spatial confinement can be caused by molecular crowding or other *in vivo* effects. The spatial confinement can destabilize the low-salt (extended) state by reducing the conformational space and consequently decrease the electrostatic free energy difference between the compact conformations and the (restricted) extended conformations (52). In addition, the tertiary contacts would further stabilize the compact state. These two effects combined together cause a reduced ion concentration required to induce the folding transition. Therefore,  $\text{Na}^+$  and  $\text{Mg}^{2+}$  are more efficient in RNA folding in a crowded environment.

## Conclusions and Discussions

In this work, we employed the newly refined TBI model (72, 73) to investigate how ions cause compaction for a system of loop-tethered helices. The main advantage of the TBI model is its ability to account for the possible ion correlation and fluctuation effects. The present study distinguishes from the previous studies (70) on similar systems in several novel aspects.

First, the present study is based on the 3D (instead of planar) rotational degrees of freedom in the conformational sampling of the system. In contrast to co-planar (2D) helix orientations, the 3D random orientation of the helices would reduce the (ensemble averaged) ion correlation effect and the associated force between the helices.

Second, the main focus of the present study is the influence of the spatial confinement and the tertiary contacts upon the ion effect and the comparisons with the the PB-based predictions and the recent experimental results. The study leads to the following main conclusions:

1.  $\text{Na}^+$  can induce a transition from an ensemble of extended conformations to an ensemble of random relaxed conformations with a flat energy landscape. In contrast,  $\text{Mg}^{2+}$  can induce a transition from an extended state to a conformation ensemble that is slightly more ordered and slightly more compact than the random relaxation conformational ensemble. However, such a  $\text{Mg}^{2+}$ -induced state is far looser than the (electrostatically) folded state. The predictions from the TBI model are in accordance with the experimental data for both  $\text{Na}^+$  and  $\text{Mg}^{2+}$  solutions, while the PB theory significantly underestimates the  $\text{Mg}^{2+}$  efficiency.
2. A tertiary contact would make the ion ( $\text{Na}^+$  and  $\text{Mg}^{2+}$ )-dependent folding transition much sharper than the tertiary contact-free case. Furthermore, stronger tertiary contacts can fold RNAs at lower ion

concentrations for both of  $\text{Na}^+$  and  $\text{Mg}^{2+}$ .

3. Spatial confinement (e.g., due to macromolecular crowding) significantly promotes the ion efficiency in mediating RNA folding for both  $\text{Na}^+$  and  $\text{Mg}^{2+}$ . The effect of the spatial confinement can be attributed to the decreased electrostatic free energy difference between the compact ensemble and the (restricted) extended ensemble.

The current theory gives overall good agreement with the experiment results, suggesting an overall reliable analysis and predictions for the ion-induced compaction and the effects of spatial confinement. Further investigation of the problem requires improvements of the model in several aspects. First, in the structural modeling, although we have taken in account the non-planar conformations, we have ignored conformations generated from the spin of the helices and the nonsymmetric rotations of the helix axes. Including these conformations may cause changes in the free energy landscape, though a detailed study for such changes requires exceedingly high computational cost. Second, the current form of the TBI model cannot treat the sequence preference in ion-binding (71, 85). The specific binding could make important contributions to the ion effect, although for the PEG-tethered helix system here, the contribution of the specific binding may be weak. Finally, we have neglected the interference from the helix on the loop conformations except for the constraint of the end-end distance  $x$ . The effect of the loop-helix interference may not be significant for a PEG loop. However, such a effect can be important for a polynucleotide loop which is highly charged.

## Acknowledgments

This research was supported by the National Science Foundation (grants MCB0920067 and MCB0920411), National Institutes of Health (grant GM063732) (to S.-J.C.), National Science Foundation of China (grants 11074191, 11175132, and 10844007), Program for New Century Excellent Talents (NCET 08-0408), Fundamental Research Funds for the Central Universities, the National Key Scientific Program (973)-Nanoscience and Nanotechnology (No. 2011CB933600) and the Scientific Research Foundation for the Returned Overseas Chinese Scholars, State Education Ministry (to Z.-J.T.).

## References

- [1] Bloomfield, V.A., D.M. Crothers, and I. Tinoco, Jr. 2000. *Nucleic Acids: Structure, Properties and Functions*. University Science Books, Sausalito, CA.
- [2] Tinoco, I., and C. Bustamante. 1999. How RNA folds. *J. Mol. Biol.* 293:271-281.
- [3] Bloomfield, V.A. 1997. DNA condensation by multivalent cations. *Biopolymers* 44:269-282.
- [4] Brion, P., and E. Westhof. 1997. Hierarchy and dynamics of RNA folding. *Annu. Rev. Biophys. Biomol. Struct.* 26:113-137.
- [5] Sosnick, T.R. and T. Pan. 2003. RNA folding: models and perspectives. *Curr. Opin. Struct. Biol.* 13:309-316.
- [6] Draper, D.E. 2008. RNA folding: thermodynamic and molecular descriptions of the roles of ions. *Biophys. J.* 95:5489-5495.
- [7] Chu, V.B., and D. Herschlag. 2008. Unwinding RNA's secrets: advances in the biology, physics, and modeling of complex RNAs. *Curr. Opin. Struct. Biol.* 18:305-314.
- [8] Chen, S.J. 2008. RNA Folding: conformational statistics, folding kinetics, and ion electrostatics. *Annu. Rev. Biophys.* 37:197-214.
- [9] Woodson, S.A. 2010. Compact intermediates in RNA folding. *Annu. Rev. Biophys.* 39:61-77.
- [10] Wong, G.C., and L. Pollack. 2010. Electrostatics of strongly charged biological polymers: ion-mediated interactions and self-organization in nucleic acids and proteins. *Annu. Rev. Phys. Chem.* 61:171-189.
- [11] Vander Meulen, K.A., S.E. Butcher. 2012. Characterization of the kinetic and thermodynamic landscape of RNA folding using a novel application of isothermal titration calorimetry *Nucleic Acids Res.* 40:2140-2151.
- [12] Stellwagen, E., J.M. Muse, N.C. Stellwagen. 2011. Monovalent cation size and DNA conformational stability. *Biochemistry* 50:3084-94.
- [13] Tan, Z.J., and S.J. Chen. 2011. Importance of diffuse metal ion binding to RNA. *Met. Ions Life Sci.* 9:101-124.
- [14] Minton, A.P. 2000. Implications of macromolecular crowding for protein assembly. *J. Biol. Chem.* 10:34-39.
- [15] Zhou, H.X., G. Rivas, and A.P. Minton. 2008. Macromolecular crowding and confinement: biochemical, biophysical, and potential physiological consequences. *Annu. Rev. Biophys.* 37:375-97.
- [16] Burz, D.S., and A. Shekhtman. 2009. Structural biology: Inside the living cell. *Nature* 458:37-8.
- [17] Lambert, D., D. Leipply, and D.E. Draper. 2010. The osmolyte TMAO stabilizes native RNA tertiary structures in the absence of  $Mg^{2+}$ : evidence for a large barrier to folding from phosphate dehydration. *J. Mol. Biol.* 404:138-57.

- [18] Pincus, D.L., C. Hyeon, and D. Thirumalai. 2008. Effects of trimethylamine N-oxide (TMAO) and crowding agents on the stability of RNA hairpins. *J. Am. Chem. Soc.* 130:7364-72.
- [19] Kilburn, D., J.H. Roh, L. Guo, R.M. Briber, S.A. Woodson. 2010. Molecular crowding stabilizes folded RNA structure by the excluded volume effect. *J. Am. Chem. Soc.* 132:8690-8696.
- [20] Zheng, K.W., Z. Chen, Y.H. Hao, and Z. Tan. 2010. Molecular crowding creates an essential environment for the formation of stable G-quadruplexes in long double-stranded DNA. *Nucleic Acids Res.* 38:327-38.
- [21] Rajendran, A., S. Nakano, and N. Sugimoto. 2010. Molecular crowding of the cosolutes induces an intramolecular i-motif structure of triplet repeat DNA oligomers at neutral pH. *Chem. Commun.* 46:1299-301.
- [22] Serra, M.J., and D.H. Turner. 1995. Predicting thermodynamic properties of RNA. *Methods Enzymol.* 259:242-261.
- [23] SantaLucia, J., Jr. 1998. A unified view of polymer, dumbbell, and oligonucleotide DNA nearest-neighbor thermodynamics. *Proc. Natl. Acad. Sci. USA* 95:1460-1465.
- [24] Xia, T., J. SantaLucia, M.E. Burkard, R. Kierzek, S.J. Schroeder, X. Jiao, C. Cox, and D.H. Turner. 1998. Thermodynamic parameters for an expanded nearest-neighbor model for formation of RNA duplexes with Watson-Crick base pairs. *Biochemistry* 37:14719-14735.
- [25] Chen, S.J., and K.A. Dill. 2000. RNA folding energy landscapes. *Proc. Natl. Acad. Sci. USA.* 97:646-651.
- [26] Zhang, W.B., and S.J. Chen. 2002. RNA hairpin-folding kinetics. *Proc. Natl. Acad. Sci. USA.* 99:1931-1936.
- [27] Zuker, M. 2003. Mfold web server for nucleic acid folding and hybridization prediction. *Nucleic Acids Res.* 31:3406-3415.
- [28] Tyagi, R., and D.H. Mathews. 2007. Predicting helical coaxial stacking in RNA multibranch loops. *RNA* 13:939-951.
- [29] Blake, R.D., and S.G. Delcourt. 1998. Thermal stability of DNA. *Nucleic Acids Res.* 26:3323-3332.
- [30] Owczarzy, R., Y. You, B.G. Moreira, J.A. Manthey, L. Huang, M. A. Behlke, and J. A. Walder. 2004. Effects of sodium ions on DNA duplex oligomers: improved predictions of melting temperatures. *Biochemistry* 43:3537-3554.
- [31] Tan, Z.J., and S.J. Chen. 2008. Salt dependence of nucleic acid hairpin stability. *Biophys. J.* 95:738-752.
- [32] Tan, Z.J., and S.J. Chen. 2007. RNA helix stability in mixed  $\text{Na}^+/\text{Mg}^{2+}$  solution. *Biophys. J.* 92:3615-3632.
- [33] Tan, Z.J., and S.J. Chen. 2006. Nucleic acid helix stability: effects of salt concentration, cation valency and size, and chain length. *Biophys. J.* 90:1175-1190.
- [34] Heilman-Miller, S.L., D. Thirumalai, and S.A. Woodson. 2001. Role of counterion condensation in folding of the Tetrahymena ribozyme. I. equilibrium stabilization by cations. *J. Mol. Biol.* 306:1157-1166.
- [35] Koculi, E, C. Hyeon, D. Thirumalai, and S.A. Woodson. 2007. Charge density of divalent metal cations determines RNA stability. *J. Am. Chem. Soc.* 129:2676-2682.

- [36] Takamoto, K., Q. He, S. Morris, M.R. Chance, and M. Brenowitz. 2002. Monovalent cations mediate formation of native tertiary structure of the *Tetrahymena thermophila* ribozyme. *Nature Struct. Biol.* 9:928-933.
- [37] Soto, A.M., V. Misra, and D.E. Draper. 2007. Tertiary structure of an RNA pseudoknot is stabilized by "diffuse" Mg<sup>2+</sup> ions. *Biochemistry* 46:2973-2983.
- [38] Kim, H.D., G.U. Nienhaus, T. Ha, J.W. Orr, J.R. Williamson, and S. Chu. 2002. Mg<sup>2+</sup>-dependent conformational change of RNA studied by fluorescence correlation and FRET on immobilized single molecules. *Proc. Natl. Acad. Sci. USA* 99:4284-4289.
- [39] Schlatterer, J.C., L.W. Kwok, J.S. Lamb, H.Y. Park, K. Andresen, M. Brenowitz, and L. Pollack. 2008. Hinge stiffness is a barrier to RNA folding. *J. Mol. Biol.* 379:859-870.
- [40] Lipfert, J., A.Y. Sim, D. Herschlag, S. Doniach. 2010. Dissecting electrostatic screening, specific ion binding, and ligand binding in an energetic model for glycine riboswitch folding. *RNA* 16:708-719.
- [41] Qiu, X., K. Andresen, L.W. Kwok, J.S. Lamb, H.Y. Park, L. Pollack. 2007. Inter-DNA attraction mediated by divalent counterions. *Phys. Rev. Lett.* 99:038104.
- [42] Qiu, X., K. Andresen, J.S. Lamb, L.W. Kwok, L. Pollack. 2008. Abrupt transition from a free, repulsive to a condensed, attractive DNA phase, induced by multivalent polyamine cations. *Phys. Rev. Lett.* 101:228101.
- [43] Bai, Y., R. Das, I. S. Millett, D. Herschlag, and S. Doniach. 2005. Probing counterion modulated repulsion and attraction between nucleic acid duplexes in solution. *Proc. Natl. Acad. Sci. USA* 102:1035C1040.
- [44] Bai, Y., V.B. Chu, J. Lipfert, V.S. Pande, D. Herschlag, S. Doniach. 2008. Critical assessment of nucleic acid electrostatics via experimental and computational investigation of an unfolded state ensemble. *J. Am. Chem. Soc.* 130:12334-12341.
- [45] Chu, V.B., J. Lipfert, Y. Bai, V.S. Pande, S. Doniach, D. Herschlag. 2009. Do conformational biases of simple helical junctions influence RNA folding stability and specificity? *RNA* 15:2195-2205.
- [46] Cheung, M.S., D. Klimov, D. Thirumalai. 2005. Molecular crowding enhances native state stability and refolding rates of globular proteins. *Proc. Natl. Acad. Sci USA.* 102:4753-8.
- [47] Kudlay, A., M.S. Cheung, D. Thirumalai. 2009. Crowding effects on the structural transitions in a flexible helical homopolymer. *Phys. Rev. Lett.* 102:118101.
- [48] Wang, W., W.X. Xu, Y. Levy, E. Trizac, P.G. Wolynes. 2009. Confinement effects on the kinetics and thermodynamics of protein dimerization. *Proc. Natl. Acad. Sci. USA* 106:5517-22.
- [49] Qin, S., and H.X. Zhou. 2009. Atomistic of macromolecular crowding predicts modest increases in folding and binding stability. *Biophys. J.* 97:12-19.
- [50] Jiao, M., H.T. Li, J. Chen, A.P. Minton, Y. Liang. 2010. Attractive protein-polymer interactions markedly alter the effect of macromolecular crowding on protein association equilibria. *Biophys. J.* 99:914-23.
- [51] Wang, Q., K.-C. Liang, A. Czader, M. N. Waxham, M. S. Cheung. 2011. The effect of macromolecular crowding, ionic strength and calcium binding on calmodulin dynamics. *PLoS Comput. Biol.* 7:e1002114.

- [52] Denesyuk, N., and D. Thirumalai. 2011. Crowding Promotes the Switch from Hairpin to Pseudoknot Conformation in Human Telomerase RNA. *J. Am. Chem. Soc.* 133:11858-11861.
- [53] Chen, A.A., M. Marucho, N.A. Baker. and R. Pappu. 2009. Simulations of RNA Interactions with Monovalent Ions. *Methods Enzymol.* 469:411-432.
- [54] Chen, A.A., D.E. Draper. and R.V. Pappu. 2009. Molecular simulation studies of monovalent counterion-mediated interactions in a model RNA kissing loop. *J. Mol. Biol.* 390:805-819.
- [55] Auffinger, P., L. Bielecki, and E. Westhof. 2003. The  $Mg^{2+}$  Binding Sites of the 5S rRNA Loop E Motif as Investigated by Molecular Dynamics Simulations. *Chem. Biol.* 10:551-561.
- [56] Dong, F., B. Olsen. and N.A. Baker. 2008. Computational Methods for Biomolecular Electrostatics. *Methods Cell Biol.* 84:843-870.
- [57] Joung, I. and T.E. Cheatham. 2009. Molecular dynamics simulations of the dynamic and energetic properties of alkali and halide ions using water-model specific ion parameters. *J. Phys. Chem. B.* 113:13279-13290.
- [58] Kirmizialtin, S., Pabit, S.A., Meisburger, S.P., Pollack, L., Elber, R. 2012 RNA and its ionic cloud: Solution scattering experiments and atomically detailed simulations *Biophys. J.* 102:819-828.
- [59] Manning, G.S. 1978. The molecular theory of polyelectrolyte solutions with applications to the electrostatic properties of polynucleotides. *Q. Rev. Biophys.* 11:179-246.
- [60] Gilson, M.K., K.A. Sharp, and B. Honig. 1987. Calculating the electrostatic potential of molecules in solution: method and error assessment. *J. Comput. Chem.* 9:327-335.
- [61] You, T.J., and S.C. Harvey. 1993. Finite element approach to the electrostatics of macromolecules with arbitrary geometries. *J. Comput. Chem.* 14:484-501.
- [62] Baker, N.A., D. Sept, S. Joseph, M.J. Holst, and J.A. McCammon. 2000. Electrostatics of nanosystems: Application to microtubules and the ribosome. *Proc. Natl. Acad. Sci. USA* 98:10037-10041.
- [63] Boschitsch, A.H., and M.O. Fenley. 2007. A new outer boundary formulation and energy corrections for the nonlinear Poisson-Boltzmann equation. *J. Comput. Chem.* 28:909-921.
- [64] Chen, D., Z. Chen, C. Chen, W. Geng, and G.W. Wei. 2011. MIBPB: A software package for electrostatic analysis. *J. Comput. Chem.* 32:756-70.
- [65] Lu, B., X. Cheng, J. Huang, and J.A. McCammon. 2010. AFMPB: An adaptive fast multipole Poisson-Boltzmann solver for calculating electrostatics in biomolecular systems. *Comput. Phys. Commun.* 181:1150-1160.
- [66] Tan, Z.J. and S.J. Chen. 2009. Predicting electrostatic forces in RNA folding. *Methods Enzymol.* 469:465-487.
- [67] Tan, Z.J., and S.J. Chen. 2005. Electrostatic correlations and fluctuations for ion binding to a finite length polyelectrolyte. *J. Chem. Phys.* 122:044903.
- [68] Grochowski, P., J. Trylska. 2008. Continuum molecular electrostatics, salt effects and counterion binding. A review of the Poisson-Boltzmann theory and its modifications. *Biopolymers* 89:93-113.



- [69] Tan, Z.J., and S.J. Chen. 2006. Ion-mediated nucleic acid helix-helix interactions. *Biophys. J.* 91:518-536.
- [70] Tan, Z.J., and S.J. Chen. 2006. Electrostatic free energy landscape for nucleic acid helix assembly. *Nucleic Acids Res.* 34:6629-6639.
- [71] Tan, Z.J., and S.J. Chen. 2008. Electrostatic free energy landscapes for DNA helix bending. *Biophys. J.* 94:3137-3149
- [72] Tan, Z.J., and S.J. Chen. 2010. Predicting ion binding properties for RNA tertiary structures. *Biophys. J.* 99:1565-1576.
- [73] Tan, Z.J., and S.J. Chen. 2011. Salt contribution to RNA tertiary folding stability. *Biophys. J.* 101:176-187.
- [74] Chen, G., Z.J. Tan, and S.J. Chen. 2010. Salt dependent folding energy landscape of RNA three-way junction. *Biophys. J.* 98:111-120.
- [75] Lu, X.J., and W.K. Olson. 2003. 3DNA: a software package for the analysis, rebuilding and visualization of three-dimensional nucleic acid structures. *Nucleic Acids Res.* 31:5108-5121.
- [76] Thirumalai, D. and B.Y. Ha. 1998. Statistical mechanics of semiflexible chains In Grosberg, A. (Ed.). Theoretical and mathematical models in polymer research, San Diego, CA Academic Press. Vol.1, pp.135.
- [77] Hyeon, C., R.T. Dima, D. Thirumalai D. 2006. Size, shape, and flexibility of RNA structures. *J. Chem. Phys.* 125:194905.
- [78] Murphy, M.C., I. Rasnik, W. Cheng, T.M. Lohman, and T. Ha. 2004. Probing single-stranded DNA conformational flexibility using fluorescence spectroscopy. *Biophys. J.* 86:2530-2537.
- [79] Walter, A.E., and D.H. Turner. 1994. Sequence dependence of stability for coaxial stacking of RNA helices with Watson-Crick base paired interfaces. *Biochemistry* 33:12715-12719.
- [80] Rau, D.C. and Parsegian, V.A. 1992. Direct measurement of the intermolecular forces between counterion-condensed DNA double helices. Evidence for long range attractive hydration forces. *Biophys. J.* 61:246-259.
- [81] Raspaud, E., Durand, D., Livolant, F. 2005. Interhelical spacing in liquid crystalline spermine and spermidine-DNA precipitates *Biophys. J.* 88:392-403.
- [82] Todd, B.A., V.A. Parsegian, A. Shirahata, T.J. Thomas, and D.C. Rau. 2008. Attractive forces between cation condensed DNA double helices. *Biophys. J.* 94:4775-4782.
- [83] Varnai, P., and Y. Timsit. 2010. Differential stability of DNA crossovers in solution mediated by divalent cations. *Nucleic Acids Res.* 38:4163-4172.
- [84] D. Svergun, C. Barberato and M. H. J. Koch. 1995. CRYSOLO-a program to evaluate X-ray solution scattering of biological macromolecules from atomic coordinates. *J. Appl. Cryst.* 28:768-773.
- [85] Stellwagen, E., Q. Dong, and N.C. Stellwagen. 2007. Quantitative analysis of monovalent counterion binding to random-sequence, double-stranded DNA using the replacement ion method. *Biochemistry* 46:2050-2058.

## FIGURE CAPTION

**FIGURE 1** The conformation of two (DNA) helices tethered by a loop can be characterized by three structural parameters: the end-to-end distance  $x$  (O-O'), the angles  $\theta$  and  $\gamma$  illustrated in the figure. The freedom of  $\gamma$  (rotation of the axis into the paper) is used to produce non-planar configurations. The P-P' distance  $R_{pp'} \leq R_{\max}$  represents the spatial restriction for the two helices due to, e.g., the macromolecular crowding effect.  $R_{cc}$  between the centers of the helices is used to quantify the compactness of the model. Tertiary contact energy can be added for conformations with a small  $R_{cc}$ . The DNA helices are constructed with the software X3DNA (75) and are displayed with the software PyMol (<http://pymol.sourceforge.net/>).

**FIGURE 2** The electrostatic free energy landscapes  $G_E(x, \theta, \gamma)$  as a function of  $[\text{Na}^+]$  (A-D) and  $[\text{Mg}^{2+}]$  (E-F). Here  $x$  is the end-to-end distance and  $\Theta$  is the angle between the two helix axes.  $\Theta$  is determined by the  $(\theta, \gamma)$  angles (see Eq. 7). The color scale represents the energy difference between the configuration  $(x, \Theta)$  and the state with the minimum free energy. From 0 to  $5 k_B T$ , the color changes gradually from Red to Blue. Note that the system is in a 16mM  $\text{Na}^+$  background due to the Na-MOPS buffer (44).

**FIGURE 3** Ion-mediated structural collapse in the absence of the tertiary contact and spatial confinement. (A, B) Ion concentration-dependence of the compactness  $\bar{R}_{cc}$  (the mean distance between the helix centers) as a function of  $\text{Na}^+$  (A) and  $\text{Mg}^{2+}$  (B). Dashed lines denote the random relaxation (fully-neutralized) state and the dotted lines denote the upper limit of the electrostatically folded state ( $\bar{R}_{cc} \sim 30\text{\AA}$ ) (69, 70, 80–82). (C,D) The SAXS profiles calculated for the different added  $\text{Na}^+$  (C) and  $\text{Mg}^{2+}$  (D). Lines are the reference SAXS profiles. Dashed lines: the upper limit of the electrostatically folded state ( $\bar{R}_{cc} \simeq 30\text{\AA}$ ); Solid lines: the random relaxation (fully-neutralized) state; Dotted lines: the extended state (with no added salts). The SAXS profiles are calculated from the software CRY SOL (84) with the statistical weight determined from the free energy  $G(x, \theta, \gamma)$ . (E,F) The “relaxed” fraction  $\chi$  as a function of  $[\text{Na}^+]$  (E) and  $[\text{Mg}^{2+}]$  (F), respectively; see Eq. 9. Symbols: the experimental data by Bai et al (44); Solid lines: the calculated results with the SAXS profiles  $I(Q)$  determined from the TBI model; Dotted lines: calculated with the compactness  $\bar{R}_{cc}$  determined from the TBI model; Dashed lines: calculated with the SAXS profiles determined from the PB theory by Bai et al (44). The “relaxed” state is taken as the fully neutralized state. Note that the system is in 16mM  $\text{Na}^+$  background due to the Na-MOPS buffer (44).

**FIGURE 4** The electrostatic free energy landscapes  $G_E(R_{cc}, R_{\max})$ , where  $R_{\max}$  represents the spatial restriction for the helices (e.g., due to the macromolecular crowding); see Eq. 10. The color scale denotes the energy difference between  $G_E(R_{cc}, R_{\max})$  and the minimum value for each  $R_{\max}$ :  $\Delta G_E = G_E(R_{cc}, R_{\max}) - G_E(R_{cc}, R_{\max})_{\min}$ . From 0 to  $5 k_B T$ , the color changes uniformly from Red to Blue.

**FIGURE 5** Ion-mediated structural folding in the presence of tertiary contact and spatial restriction. (A,B) The compactness  $\bar{R}_{cc}$  of the loop-tethered helices as functions of  $[\text{Na}^+]$  (A) and  $[\text{Mg}^{2+}]$  (B) for the different  $R_{\max}$  values (from the right to the left:  $120\text{\AA}$ ,  $82\text{\AA}$ ,  $78\text{\AA}$ , and  $70\text{\AA}$ ) and the different tertiary

contact energy  $g_{3^\circ}$  (solid lines:  $-10k_B T$ , and dashed lines:  $-14 k_B T$ ). (C,D) The folded fraction  $f_{\text{folded}}$  as a function of  $[\text{Na}^+]$  (C) and  $[\text{Mg}^{2+}]$  (D) for the different  $R_{\text{max}}$  values (from the right to the left:  $120\text{\AA}$ ,  $82\text{\AA}$ ,  $78\text{\AA}$  and  $70\text{\AA}$ ) and the different tertiary contact energy  $g_{3^\circ}$  (solid lines:  $-10k_B T$ , and dashed lines:  $-14 k_B T$ ). (E,F) The ion concentration midpoints for the folding transition as a function of  $R_{\text{max}}$  and the different tertiary contact energies  $g_{3^\circ}$ . From the top to the bottom:  $g_{3^\circ} = -10k_B T$ ,  $-12k_B T$ , and  $-14k_B T$ , respectively.

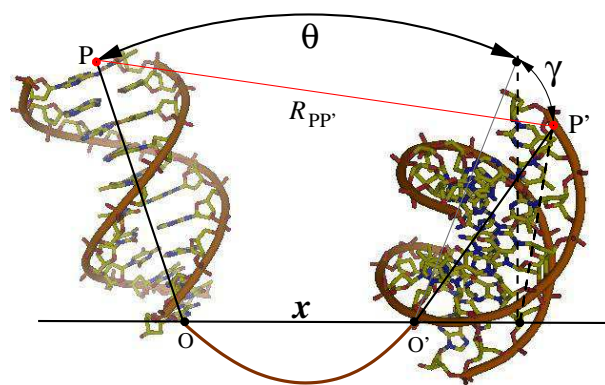


Figure 1:

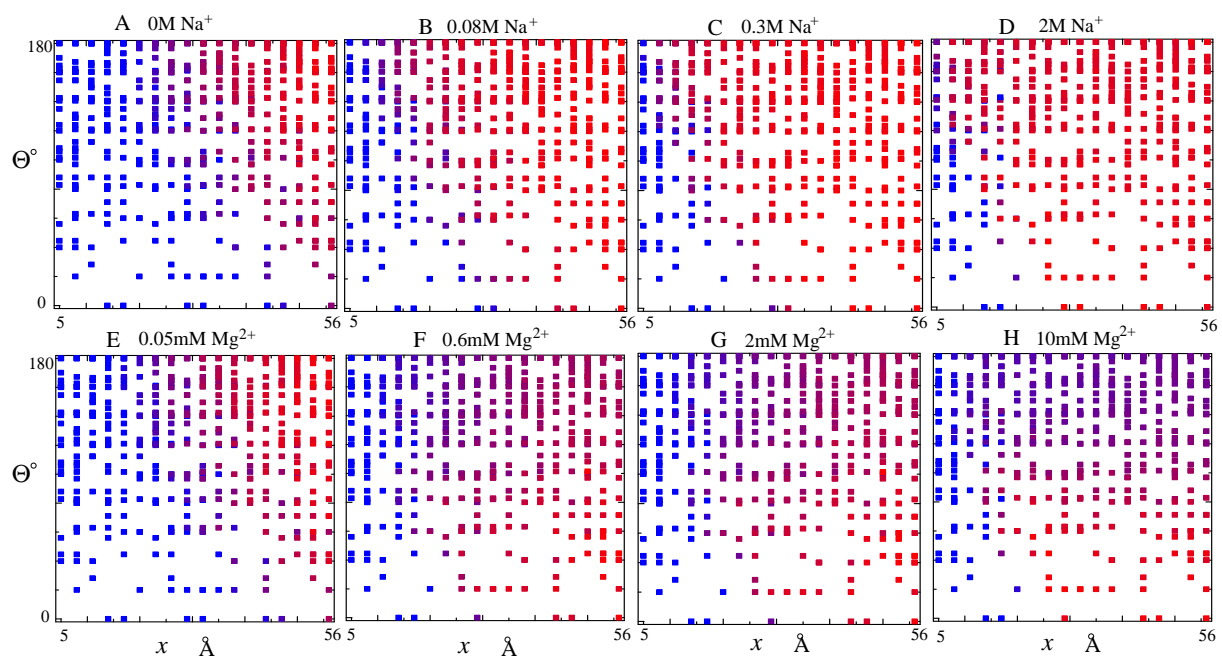


Figure 2:

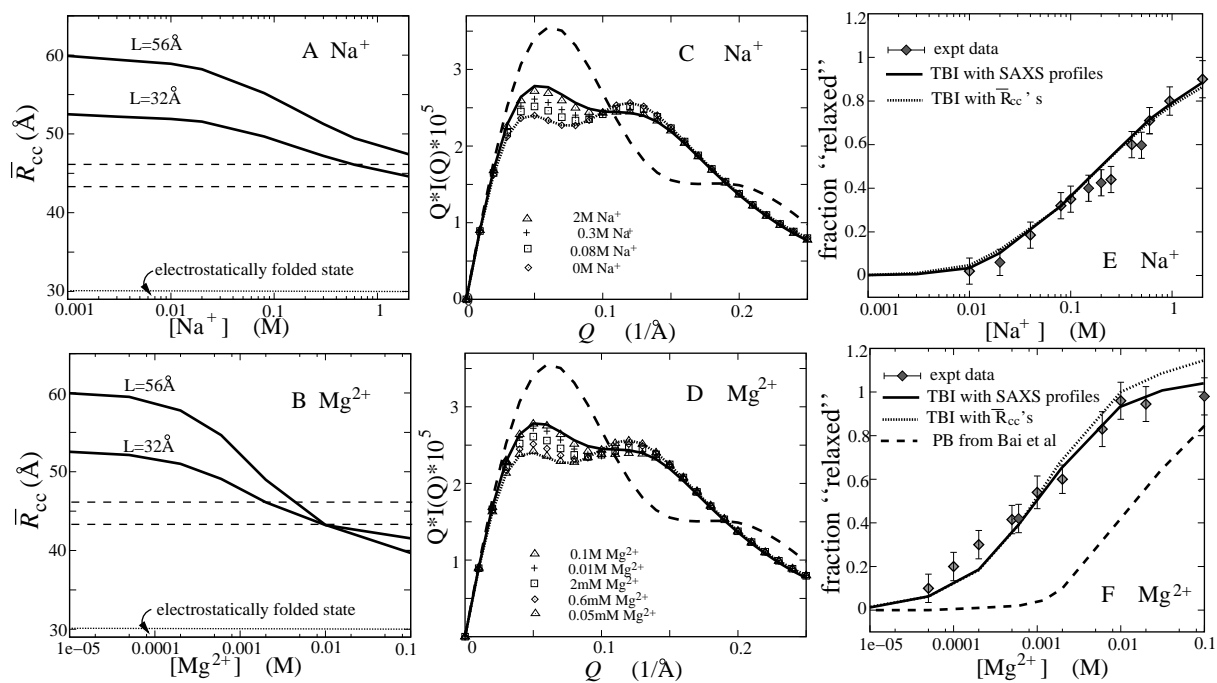


Figure 3:



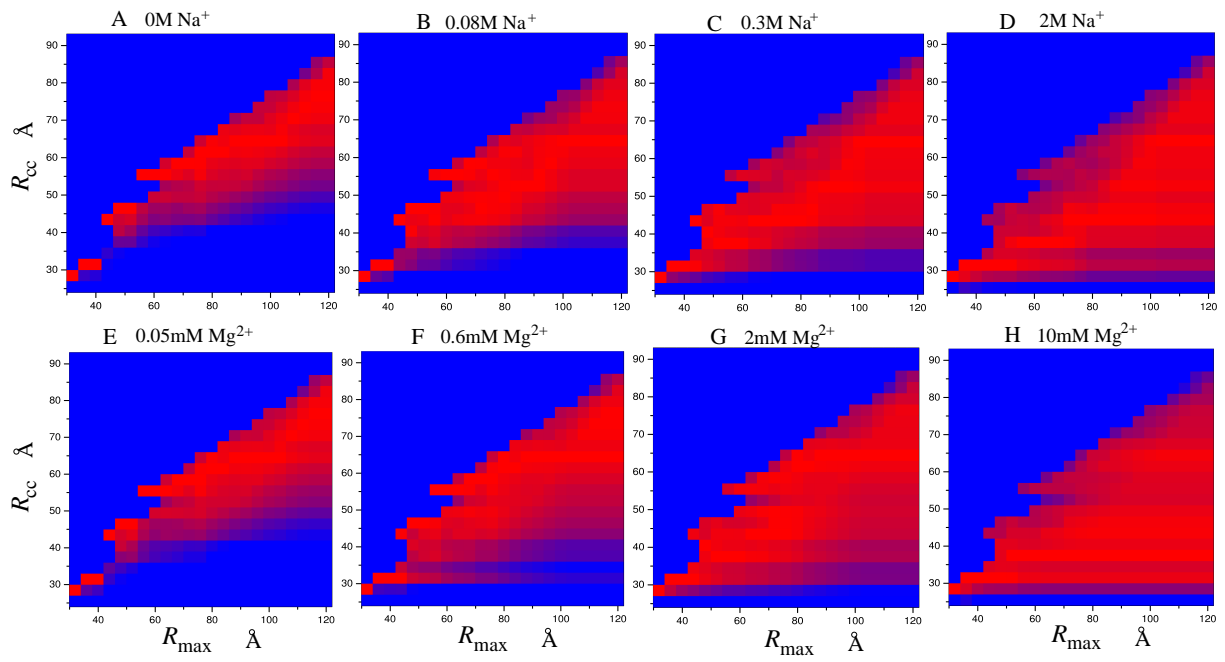


Figure 4:

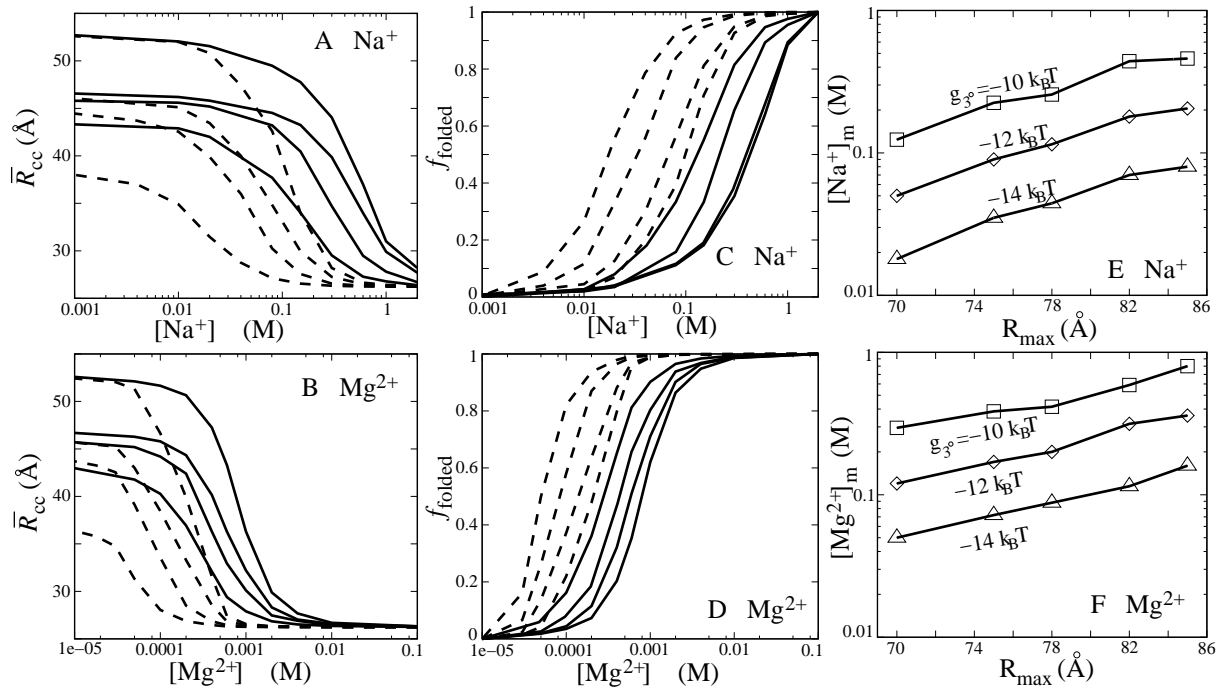


Figure 5: